

# Multi-spectral sirens: Gravitational-wave cosmology with (multi-) sub-populations of binary black holes

YIN-JIE LI (李银杰) <sup>1</sup>, SHAO-PENG TANG (唐少鹏) <sup>1</sup>, YUAN-ZHU WANG (王远瞩) <sup>2,1</sup> AND  
YI-ZHONG FAN (范一中) <sup>1,3</sup>

<sup>1</sup>Key Laboratory of Dark Matter and Space Astronomy, Purple Mountain Observatory, Chinese Academy of Sciences, Nanjing 210023, People's Republic of China

<sup>2</sup>Institute for theoretical physics and cosmology, Zhejiang University of Technology, Hangzhou, 310032, People's Republic of China

<sup>3</sup>School of Astronomy and Space Science, University of Science and Technology of China, Hefei, Anhui 230026, People's Republic of China

## ABSTRACT

The cosmic expansion rate can be directly measured with gravitational wave (GW) data of the compact binary mergers, by jointly constraining the mass function of the population and the cosmological model via the so called spectral sirens. Such a method relies on the features in the mass functions, which may originate from some individual sub-populations, and hence become blurred/indistinct due to the superposition of different sub-populations. In this work we propose a novel approach to constrain the cosmic expansion rate with sub-populations of GW events, named multi-spectral sirens. We illustrate the advantage of the multi-spectral sirens compared to the traditional spectral sirens by simulation with mock data. The application of this approach to the GWTC-3 data yields  $H_0 = 73.25^{+29.87}_{-25.55}$  Mpc<sup>-1</sup> km s<sup>-1</sup> (median and symmetric 68.3% credible level). The incorporation of the bright standard siren GW170817 with a uniform prior in [10,200] Mpc<sup>-1</sup> km s<sup>-1</sup> gives  $H_0 = 72.38^{+15.03}_{-9.13}$  Mpc<sup>-1</sup> km s<sup>-1</sup> (68.3% confidence level), corresponding to an improvement of  $\sim 28\%$  with respect to the measurement from sole GW170817.

## 1. INTRODUCTION

The discrepancy in the values of the Hubble constant as determined by early and late Universe observations (Planck Collaboration et al. 2016; Riess et al. 2019; Verde et al. 2019) has garnered significant attention over the past decade and remains unresolved. Gravitational waves (GWs) from coalescing compact binaries (CBCs) provide measurements of the luminosity distances of sources. When combined with redshift information, these measurements can constrain cosmological models (Schutz 1986; Holz & Hughes 2005). The first GW detection from a binary neutron star (NS) merger, GW170817 (Abbott et al. 2017a), was accompanied by electromagnetic observations (Abbott et al. 2017b) that provided a redshift measurement, enabling a direct estimate of the Hubble constant  $H_0$  (Abbott et al. 2017c). Additionally, GWs from CBCs alone can also constrain cosmological models through the use of so-called spectral sirens (Taylor et al. 2012; Farr et al. 2019; You et al. 2021; Mastrogiovanni et al. 2021; Ezquiaga & Holz 2022; Abbott et al. 2023a; Magaña Hernandez & Ray 2024; Farah et al. 2024). For this method, distinct and recognizable features in the CBC mass functions are advantageous for precise measurement. These features include, e.g., the lower-mass gap between the heaviest NSs and the lightest black holes (BHs) (Rhoades & Ruffini 1974; Kalogera & Baym 1996; Bailyn et al. 1998; Özel et al. 2010; Farr et al. 2011; Li et al. 2021a; Farah et al. 2022), as well as the higher-mass gap resulting from (pulsational) pair-instability supernova (PPISN) explosions (Woosley 2017; Woosley & Heger 2021), subsequently referred to here as the pair-instability mass gap (PIMG).

However, these features in the mass functions may be indistinct due to the superposition of sub-populations from different formation channels (Zevin et al. 2021; Li et al. 2022; Tiwari 2022; Cheng et al. 2023; Godfrey et al. 2023). For instance, the PIMG could be populated by hierarchical mergers (Kimball et al. 2021; Wang et al. 2022; Li et al.

2023; Pierra et al. 2024a), which may blur its lower edge and make it indistinguishable (Wang et al. 2021; Abbott et al. 2021a, 2023b). Hence, it will significantly limit the application of the spectral sirens method.

In this work, we introduce a multi-spectral sirens method which decomposes the mass spectra of sub-populations from the overall population of BBHs/BHs, to make the features in the mass function more sharp/distinct, thereby improving the measurement of cosmological parameters. Sub-populations of BBHs/BHs can be identified through the analysis of additional parameters such as spins and redshifts (Zevin et al. 2021; Gerosa & Fishbach 2021). This allows for clearer identification of features in the mass functions of these sub-populations, which in turn improves the capability of spectral sirens in measuring cosmological parameters. Our previous investigations (Li et al. 2023) have successfully identified two distinct sub-populations of BHs within the GWTC-3 dataset (Abbott et al. 2019, 2021b; The LIGO Scientific Collaboration et al. 2021a,b), employing semi-parametric models (see also Wang et al. 2022, for astrophysically motivated analysis). The first sub-population exhibits a sharp cut-off at  $\sim 40M_\odot$ , consistent with the PIMG (Farmer et al. 2019). The second sub-population features a distinct spin-magnitude distribution (peaking at approximately 0.7), suggesting origins from hierarchical mergers (Fishbach et al. 2017; Gerosa & Berti 2017). These findings have been corroborated by subsequent studies (e.g., Li et al. 2024; Pierra et al. 2024a; Guo et al. 2024).

The remainder of the article is organized as follows: Section 2 introduces the analysis framework and the novel population model employed for multi-spectral sirens. Section 3 discusses the enhancements of multi-spectral sirens over traditional spectral sirens. In Section 4, we present the results constrained by the GWTC-3 data. Discussions are provided in Section 5.

## 2. METHODS

### 2.1. Population models

Flexible mixture models are well-suited for modeling sub-populations of BHs (Li et al. 2023; Godfrey et al. 2023; Li et al. 2024). In this study, we use a basic mixture model which fits the sub-populations within the component-mass versus spin-magnitude distribution (Li et al. 2023). When the data get significantly enriched, one can use more sophisticated mixture models, e.g., models that incorporate the mass versus spin-orientation distribution (refer to the Supplementary of Li et al. (2023) and also see (Godfrey et al. 2023; Li et al. 2024)) and the mass versus spin versus redshift distribution (Guo et al. 2024).

Employing a mixture model with an adequate number of components is beneficial when dealing with distinct sub-populations, as represented by

$$\pi(m, \chi|\mathbf{\Lambda}) = \sum_{i=1}^n \pi_i(m|\mathbf{\Lambda})\pi_i(\chi|\mathbf{\Lambda})r_i, \quad (1)$$

where  $m$  and  $\chi$  denote the source-frame component mass and spin magnitude, respectively, while  $r_i$  represents the mixture fraction of the  $i$ -th sub-population. According to recent studies (Li et al. 2023), for the currently available data, a model with two components ( $n = 2$ ) adequately captures the distribution of component mass versus spin magnitude.

In light of the data from GWTC-3, we adopt a non-parametric approach to model the component-mass distribution, which mitigates the systematic uncertainty that would otherwise arise from mis-modeling of parametric model. For this purpose, we utilize the POWERLAWSPLINE model (Edelman et al. 2022), since it has a concise formula, which reads,

$$\pi_i(m|\mathbf{\Lambda}_i) = \mathcal{PS}(m|\alpha_i, m_{\min,i}, m_{\max,i}, \delta_{\text{low},i}, \delta_{\text{up},i}, f_i(m; \{f_i^j\}_{j=0}^{N_{\text{knot}}})) . \quad (2)$$

Here,  $m_{\min,i}$  and  $m_{\max,i}$  are the minimum and maximum mass cut-offs,  $\alpha_i$  is slope index,  $\delta_{\text{low},i}$  and  $\delta_{\text{up},i}$  are the smooth scale at lower and upper edges, respectively. Following Edelman et al. (2022), we use 15 knots located linearly in the logarithm space within  $[5, 100] M_\odot$  for the perturbation function  $f_i$ , and restrict the perturbation to zero at the minimum and maximum knots. The spin-magnitude distribution for  $i$ -th component is  $\pi_i(\chi|\mathbf{\Lambda}_i) = \mathcal{G}(\chi|\mu_{\chi,i}, \sigma_{\chi,i}, 0, 1)$ , a truncated Gaussian with peak  $\mu_{\chi,i}$  and width  $\sigma_{\chi,i}$  bounded in  $[0,1]$ . Then the overall population model reads

$$\pi(\lambda|\mathbf{\Lambda}) = A(\mathbf{\Lambda})p(m_2/m_1|\mathbf{\Lambda})\pi(m_1, \chi_1|\mathbf{\Lambda})\pi(m_2, \chi_2|\mathbf{\Lambda})\pi(\cos \theta_1, \cos \theta_2|\mathbf{\Lambda}) \quad (3)$$

where  $A(\mathbf{\Lambda})$  is the normalization factor,  $p(m_2/m_1|\mathbf{\Lambda})$  is the pairing function. Note that the pairing function may also be total-mass dependent (O’Leary et al. 2016), however, it is vastly degenerated with the component-mass function (Fishbach & Holz 2020). Therefore, we only account for the mass-ratio dependent pairing function, since the ignorance

of the total-mass dependent pairing have little effect on the inferred mass distribution for current data (Wang et al. 2022). The spin-orientation distribution is the same as DEFAULTSPIN model of Abbott et al. (2023b), i.e.,

$$\pi(\cos\theta_1, \cos\theta_2|\zeta, \sigma_t) = \mathcal{U}(\cos\theta_1, \cos\theta_2| -1, 1)(1 - \zeta) + \mathcal{G}(\cos\theta_1, \cos\theta_2|1, \sigma_t, -1, 1)\zeta, \quad (4)$$

where  $\mathcal{U}$  is a uniform distribution within  $(-1, 1)$ ,  $\zeta$  is the mixture fraction of the nearly-aligned assembly.

Following Abbott et al. (2023a), the merger rate density as a function of redshift reads (Madau & Dickinson 2014),

$$R(z|\gamma, \kappa, z_p) = [(1 + z_p)^{(\gamma+\kappa)} + 1](1 + z)^\gamma / [(1 + z)^{(\gamma+\kappa)} + (1 + z_p)^{(\gamma+\kappa)}]. \quad (5)$$

It is characterized by a low-redshift power-law slope  $\gamma$ , a peak at redshift  $z_p$ , and a high-redshift power-law slope  $\kappa$  after the peak. Therefore the redshift distribution of BBHs is,

$$\pi(z|\gamma, \kappa, z_p, H_0, \Omega_m) = \Phi_c \frac{dV_c(H_0, \Omega_m)}{(1 + z)dz} R(z|\gamma, \kappa, z_p), \quad (6)$$

where  $V_c$  is the comoving volume, and  $\Phi_c$  is the normalization constant. All the descriptions of the hyper-parameters and the priors are summarized in Table 1.

## 2.2. Cosmological model

We use a flat  $\Lambda$ CDM cosmological model in this work, and assume the dark energy density is constant during the cosmic expansion. Then the function of luminosity distance  $D_L$  and redshift  $z$  is represented as (Abbott et al. 2023a)

$$D_L(z) = \frac{c(1 + z)}{H_0} \int_0^z [\Omega_m(1 + x)^3 + 1 - \Omega_m]^{-1/2} dx = F(z|H_0, \Omega_m), \quad (7)$$

where  $\Omega_m$  is the present-day dimensionless matter density, and  $H_0$  is the Hubble constant. The GW signal enables the measurement of detector-frame masses of BBHs and the luminosity distance (i.e.,  $M_1, M_2, D_L$ ). Subsequently, the cosmology (with parameters  $H_0$  and  $\Omega_m$ ) allow for the calculation of source-frame masses. These are determined by the formula  $m_{1,2} = M_{1,2}/(1 + z(D_L)) = M_{1,2}/(1 + F^{-1}(D_L|H_0, \Omega_m))$ . Note that the direct measurements obtained from a GW event are the detector-frame masses and the luminosity distance. Therefore, when calculating the detection fraction  $\xi(\mathbf{\Lambda})$ , one should convert the  $(m_1, m_2, z)$  distribution to  $\pi(M_1, M_2, D_L) \propto \pi(m_1, m_2, z)(1 + z)^2 / \frac{\partial D_L}{\partial z}$ .

## 2.3. Hierarchical inference framework

We use hierarchical Bayesian inference to jointly fit the source population and cosmological models. For the given data  $\{d\}$  from  $N_{\text{det}}$  GW detections, the likelihood (Abbott et al. 2023b) for the hyperparameters  $\mathbf{\Lambda}$  is

$$\mathcal{L}(\{d\}|\mathbf{\Lambda}) \propto N^{N_{\text{det}}} e^{-N\xi(\mathbf{\Lambda})} \prod_{i=1}^{N_{\text{det}}} \int \mathcal{L}(d_i|\theta_i)\pi(\theta_i|\mathbf{\Lambda})d\theta_i, \quad (8)$$

where  $N$  is the number of mergers over the surveyed space-time volume, and  $\xi(\mathbf{\Lambda})$  means the detection fraction. The methodology for computing  $\mathcal{L}(d_i|\theta_i)$  and  $\xi(\mathbf{\Lambda})$  is detailed in Abbott et al. (2021a). It should be noted that we do not incorporate the spin-dependent selection bias, which is considered to have a negligible effect on our results (refer to Galaudage et al. (2021) and Li et al. (2023) for a comprehensive discussion). For the estimation of the posterior distributions of the hyper-parameters, we employ the *PyMultinest* sampler Buchner (2016).

## 3. SIMULATION WITH MOCK DATA

In this section, we conduct simulations using synthetic data to demonstrate the enhancements achieved by multi-spectral sirens compared to traditional spectral sirens. Our analysis primarily targets the lower-edge of the PIMG (Karathanasis et al. 2023), a typical feature used in spectral sirens, for measuring cosmological parameters (Farr et al. 2019; Ezquiaga & Holz 2022). Additionally, potential features associated with various sub-populations or formation channels (Wang et al. 2022; Godfrey et al. 2023; Ray et al. 2024; Li et al. 2024) may appear in the BH mass function (Toubiana et al. 2023; Tiwari 2024; Farah et al. 2023), which could provide more available features and offer further opportunities for multi-spectral sirens. Here, we employ two simplified truncated PowerLaw distributions to model the mass distributions BHs in two distinct sub-populations: the first-generation BHs, ranging from  $5M_\odot$  to  $40M_\odot$  with

**Table 1.** Hyper-parameters and Priors for the population and cosmological models

Descriptions	parameters	priors	
		1st component	2nd component
slope index of the mass function	$\alpha_i$	U(-4,8)	U(-4,8)
smooth scale of the $i$ -th mass lower edge	$\delta_{\text{low},i}[M_\odot]$	U(1,10)	U(1,10)
smooth scale of the $i$ -th mass upper edge	$\delta_{\text{up},i}[M_\odot]$	U(1,10)	U(1,10)
minimum mass of the $i$ -th mass function	$m_{\text{min},i}[M_\odot]$	U(2,60)	U(2,60)
maximum mass of the $i$ -th mass function	$m_{\text{max},i}[M_\odot]$	U(20,100)	U(20,100)
interpolation values of perturbation for $i$ -th mass function	$\{f_i^j\}_{j=2}^{14}$	$\mathcal{N}(0, 1)$	$\mathcal{N}(0, 1)$
mass constraints		$m_{\text{max},i} - m_{\text{min},i} > 20M_\odot$	
mean of $\chi$ distribution in $i$ -th component	$\mu_{\chi,i}$	U(0,1)	U(0,1)
standard deviation of $\chi$ distribution in $i$ -th component	$\sigma_{\chi,i}$	U(0.05, 0.5)	U(0.05, 0.5)
spin constraints		$\chi_{\text{max},i} > \mu_{\chi,i} > \chi_{\text{min},i}$	
mixing fraction of the $i$ -th component	$r_i$	$\mathcal{D}$	
standard deviation of nearly aligned $\cos\theta$	$\sigma_t$	U(0.1, 4)	
mixing fraction of nearly aligned assembly	$\zeta$	U(0,1)	
pairing function	$\beta$	U(0,8)	
local merger rate density	$R_0[\text{Gpc}^{-3}\text{yr}^{-1}]$	U(0,100)	
Hubble constant	$H_0[\text{km s}^{-1} \text{Mpc}^{-1}]$	U(10,200)	
present-day dimensionless matter densities	$\Omega_m$	U(0,1)	
slope of the powerlaw regime for the rate evolution before the point $z_p$	$\gamma$	U(0,12)	
slope of the powerlaw regime for the rate evolution after the point $z_p$	$\kappa$	U(0,6)	
redshift turning point between the power-law regimes with $\gamma$ and $\kappa$	$z_p$	U(0,4)	

**Note.** Here, U ( $\mathcal{N}$ ) represents the uniform (normal) distribution, and  $\mathcal{D}$  is for the Dirichlet distribution.

a power-law index of  $-2.1$ , and the higher-generation BHs, spanning from  $30M_\odot$  to  $80M_\odot$  with a power-law index of  $-1.5$ . The underlying (unpaired) higher-generation sub-population takes a fraction of 5%, and the pairing function is  $\propto (m_2/m_1)^{2.7}$ . Note that these configurations are consistent with the results from GWTC-3 (Li et al. 2023).

The spin-magnitude distribution of the first (second) sub-population is a truncated Gaussian with peak at 0.1 (0.7) and width of 0.15 bounded within (0,1). The spin-orientation distribution for the total BBH population is described by Eq. 4. For simplicity, we adopt  $\zeta = 1$  and  $\sigma_t = 1$ , since in this work we do not focus on the sub-populations distinguished by spin-orientation distributions. The redshift distribution is described by Eq. 6, with parameters  $\gamma = 2.7$ ,  $\kappa = 3$ ,  $z_p = 2$ ,  $H_0 = 70\text{Mpc}^{-1} \text{km s}^{-1}$ , and  $\Omega_m = 0.3$ .

We perform simulations subject to the upcoming data from the fourth observing run (O4) of LIGO-Virgo-KAGRA collaboration, which is anticipated to yield  $\sim 300$  detections (Abbott et al. 2018). In practice, we only incorporate the two advanced LIGO detectors and the advanced Virgo detector since these detectors mainly contribute to the GW detection (see the *Observing Scenario* for details). The sensitivity curves used for simulations are adopted from LIGO Document (Abbott et al. 2018). In this work we use the `aligo_O4high` and `avirgo_O4high_NEW` files. Besides, we use the Python package `GWFast` (Iacovelli et al. 2022a,b) and the `IMRPhenomXPHM` waveform (Pratten et al. 2021) to calculate the signal-to-noise ratios (SNRs) for the mock events, and we adopt a threshold of network SNR  $> 11$  to select the mock detections. For the parameter estimation of the selected events, we rapidly generate the samples from the corresponding Fisher matrix computed by `GWFast`.

For comparative analysis, we employ two models to recover the mock injections. The first model, referred to as the TwoSpin model, incorporates two sub-populations, each characterized by independent spin-magnitude distributions. The second model, named the NoSpin model, does not differentiate between sub-populations and thus does not model spin distributions. The TwoSpin model has the same formula as Eq. 3, but employs a simpler component-mass function,  $\pi_i(m|\mathbf{A}) = \mathcal{P}\mathcal{L}(m|m_{\text{min},i}, m_{\text{max},i}, \alpha_i)$  (i.e., the same as the injected mock population). To ensure a fair comparison—‘apples to apples’—we configured the NoSpin model to use the same mass function formula as the

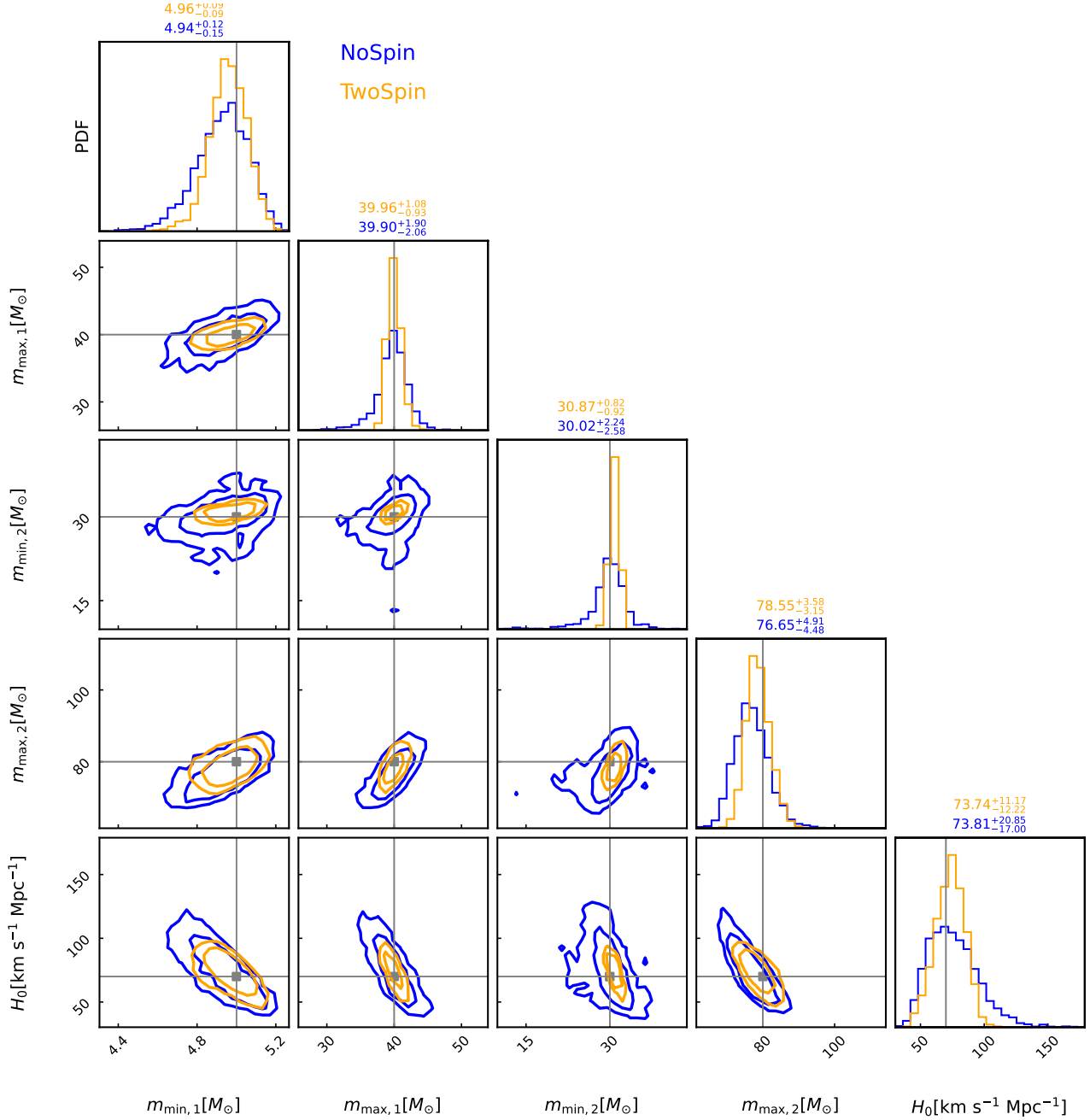


**Figure 1.** Hubble constant and the parameters for the population models recovered by the TwoSpin (in orange) and NoSpin (in blue) models with 300 mock detections in O4. The solid lines represent the injections, the contours mark the central 50% and 90% posterior credible regions, respectively; the values are for 68.3% credible intervals.

TwoSpin model. Practically, the NoSpin model represents a reduced version of the TwoSpin model, where  $\pi_i(\chi) = 1$  and  $\pi(\cos\theta_1, \cos\theta_2) = 1/4$ .

Figure 1 displays the recovered Hubble constants and population parameters for both models. The results indicate that the Hubble constant ( $H_0$ ) inferred using the TwoSpin model is approximately 40% more precise than that inferred with the NoSpin model. This enhanced precision is attributed to the more effective differentiation of the two sub-populations by the TwoSpin model, which clearly delineates the upper edge of the first sub-population and the lower edge of the second sub-population in the multi-spectral sirens, as shown in Figure 1. This distinction significantly contributes to the accuracy of the  $H_0$  measurement.

## 4. CONSTRAINTS WITH GWTC-3

Following [Abbott et al. \(2023a\)](#), we restrict our main analysis to BBH events with SNRs > 11, resulting in a total of 42 events. Notably, we exclude GW190814 ([Abbott et al. 2020](#)) due to its classification as a population outlier ([Abbott et al. 2021a](#)). We also use a supplementary catalog of BBHs with SNRs > 10 for further analysis, as illustrated in Figure 7 in the Appendix. It should be noted that the posterior samples used are not cosmologically reweighted, and are available at <https://zenodo.org/records/8177023>. The injection campaign data utilized for calculating selection effects can be accessed at [zenodo](#) ([The LIGO & collaborations 2021](#)). We begin by reproducing the results of [Abbott et al. \(2023a\)](#) with their POWERLAW+PEAK (PP) model to ensure the consistency of our framework with theirs. The corresponding posterior distribution is presented in Appendix B, confirming that our reproduced results align with those of [Abbott et al. \(2023a\)](#).

We use the Eq. 3 as the multi-spectral sirens model to jointly infer the cosmological parameters and BBH population. Following [Li et al. \(2023\)](#), we choose a two-component mixture model for Eq. 1<sup>1</sup>. This is a flexible and non-parametric model, which can mitigate the systematic uncertainty of mismodeling ([Pierra et al. 2024b](#)). We obtain  $H_0 = 73.25^{+29.87}_{-25.55}({}^{+51.65}_{-40.56})$  Mpc<sup>-1</sup> km s<sup>-1</sup> at 68.3% (90%) credible level (C.L.). Besides, we also adopt the POWERLAW+SPLINE (PS) model ([Edelman et al. 2022](#); [Abbott et al. 2023b](#)) as a traditional spectral sirens for comparison. Figure 2 shows the Hubble constants inferred with multi-spectral sirens (i.e., TwoSpin model) and traditional spectral sirens (i.e., PP and PS models). We find that the  $H_0$  measured with TwoSpin model is slightly more consistent with the two referred measurements compared to that inferred with the PP/PS model ([Abbott et al. 2023a](#)).

With the multi-spectral sirens model, we simultaneously identified two sub-populations of BHs, similar to those found in [Li et al. \(2023\)](#), see Figure 6. The maximum mass of the first sub-population (i.e., constrained to  $\sim 40M_\odot$ ) has contributed to the measurement of cosmology parameters, which is potentially associated with the lower edge of PIMG ([Li et al. 2023](#)). This feature is not incorporated into the single-population model (e.g. [Abbott et al. 2023b](#)), hence can not contribute to traditional spectral sirens ([Abbott et al. 2023a](#); [Farah et al. 2024](#); [Magaña Hernandez & Ray 2024](#)). We note the  $m_{\max,1}$  has a tail extend to high-mass range, which is resulted from the flexibility of the POWERLAW+SPLINE mass function (see also [Li et al. \(2023\)](#) for illustration). However the mass of 99% and 99.5% for the first sub-population is better measured and more degenerated with  $H_0$ , see Figure 5.

We also combine the  $H_0$  posteriors from the multi-spectral sirens and spectral sirens with the  $H_0$  inferred from the bright standard siren GW170817 ([Abbott et al. 2017c](#)) (see Figure 3), and obtain  $H_0 = 72.4^{+15.0}_{-9.1}$  Mpc<sup>-1</sup> km s<sup>-1</sup> and  $H_0 = 70.8^{+15.6}_{-9.1}$  Mpc<sup>-1</sup> km s<sup>-1</sup> (68.3% highest density interval with a uniform prior in [10, 200] Mpc<sup>-1</sup> km s<sup>-1</sup>) for the TwoSpin model and PP model, respectively. This combined measurement with multi-spectral sirens is about 28% better than the measurement from bright standard siren GW170817 alone ([Abbott et al. 2017c](#)). seems that the combined measurement (with multi-spectral sirens) of  $H_0$  shows slightly more preference for the measurement in the local universe ([Riess et al. 2019](#)), consistent with the results measured with combination of the standard siren GW170817 and the afterglow of GRB170817A ([Wang et al. 2023](#)).

## 5. SUMMARY AND DISCUSSION

We constrain the parameters of the cosmological model with mass functions of sub-populations of BBHs/BHs (i.e., via multi-spectral sirens), and illustrate the advantage of the multi-spectral sirens with a simulation study. The mock population includes two sub-populations with different spin-magnitude distributions, which are consistent with the findings in GWTC-3 ([Li et al. 2023](#)). With the identification of the second sub-population (higher-generation BHs), the first sub-population (first-generation BHs) presents a more clear cut-off/drop, which potentially enhance the measurement of cosmological parameters. Then we apply this novel multi-spectral sirens to the real data analysis with GWTC-3 ([Abbott et al. 2023a](#)), and obtain  $H_0 = 73.25^{+29.87}_{-25.55}({}^{+51.65}_{-40.56})$  Mpc<sup>-1</sup> km s<sup>-1</sup> at 68.3% (90%) C.L. Further analysis, incorporating the bright standard siren GW170817 ([Abbott et al. 2017c](#)) with a uniform prior ranging from 10 to 200, improved the precision of our estimate to  $H_0 = 72.38^{+15.03}_{-9.13}$  Mpc<sup>-1</sup> km s<sup>-1</sup> at the 68.3% HDI, which represents a 28% enhancement in precision over the measurement derived solely from GW170817.

In our mock data study, we only focus on the constraint on the Hubble constant attribute to the lower-edge of the PIMG ([Farr et al. 2019](#)). In reality, the features could be more complex. For example, the mass distribution will evolve with redshift since the metallicity of BBH progenitor systems changes with the age of the universe ([Mapelli](#)

<sup>1</sup> It is sufficient for currently available data, and a more complex mixture model may be needed when the data are significantly enriched, see [Li et al. \(2023\)](#) for detailed illustration.



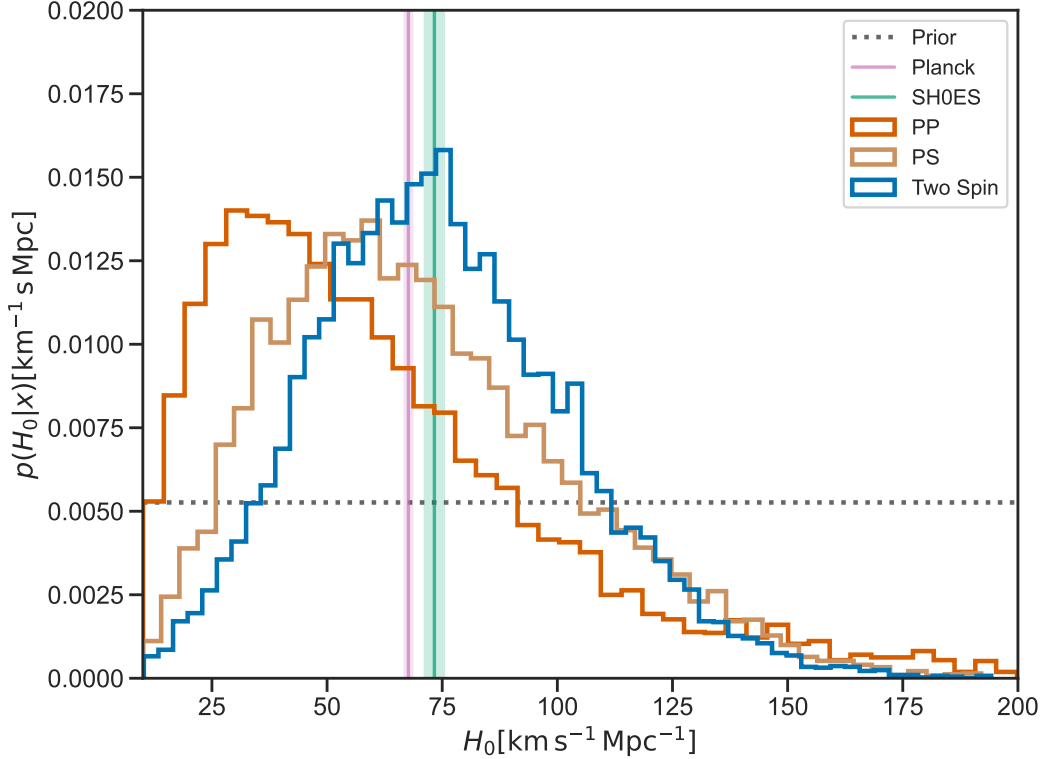


**Figure 2.** The Hubble constant inferred using multi-spectral sirens, i.e., the TwoSpin model and the traditional spectral sirens (PP and PS models), with 42 events (SNRs > 11). For reference, the pink and green bands represent the Hubble constant measured from CMB (Planck Collaboration et al. 2020) and that measured in the local universe (Riess et al. 2019), respectively. The dotted line represent the prior distribution.

et al. 2017; Vink et al. 2021). Such evolution, however, can be simultaneously constrained, unless all features in the full mass distribution evolve with the same behavior (Ezquiaga & Holz 2022). Moreover, additional features in the (sub-population) mass functions may present, like the peaks/bumps and gaps (Li et al. 2021b; Toubiana et al. 2023; Farah et al. 2023; Tiwari 2022, 2024; Callister & Farr 2024). The previously found excesses at around  $10M_{\odot}$  and  $32M_{\odot}$  (Abbott et al. 2023b) may be associated with diverse sub-populations originated from the isolated field evolution and dynamical formation channels, respectively (Godfrey et al. 2023; Ray et al. 2024; Li et al. 2024). The identification of these sub-populations will also potentially enhance the advantage of the multi-spectral sirens. However, there is still vast uncertainty with currently available data (see e.g., Godfrey et al. 2023; Li et al. 2024). Ezquiaga & Holz (2022) suggested that the expected low-mass gap (LMG, Rhoades & Ruffini 1974; Kalogera & Baym 1996; Bailyn et al. 1998; Özel et al. 2010; Farr et al. 2011) will play a dominant role on spectral sirens in era of next-generation GW detectors. However, the LMG is now found populated with unknown-origin sources (Abbott et al. 2020; The LIGO Scientific Collaboration et al. 2024). It is possible that the events in the LMG, may suffer from some unconventional evolution paths, e.g., the hierarchical mergers (Gupta et al. 2020) and/or super-Eddington accretion (Gao et al. 2022), which is identifiable by their distinctive spin properties.

In our analysis, the spin-magnitude distributions are adequately represented using simple Gaussian models, which suffice given the current data (see Supplemental Material of Li et al. 2023, for detailed illustration). However, more sophisticated models, such as non-parametric ones including auto-regressive processes (Callister & Farr 2024) and splines (Golomb & Talbot 2023; Godfrey et al. 2023), could be necessary as data sets become more comprehensive. Additionally, we have not differentiated between redshift distributions across various sub-populations due to the limited data presently available. This aspect will be included in the analysis of future data (Abbott et al. 2018).

In the final stage of this work, there was a work appeared online (Ulrich et al. 2024), where the authors investigate the generations in the BBH populations, and then apply their population model to constrain the Hubble constant

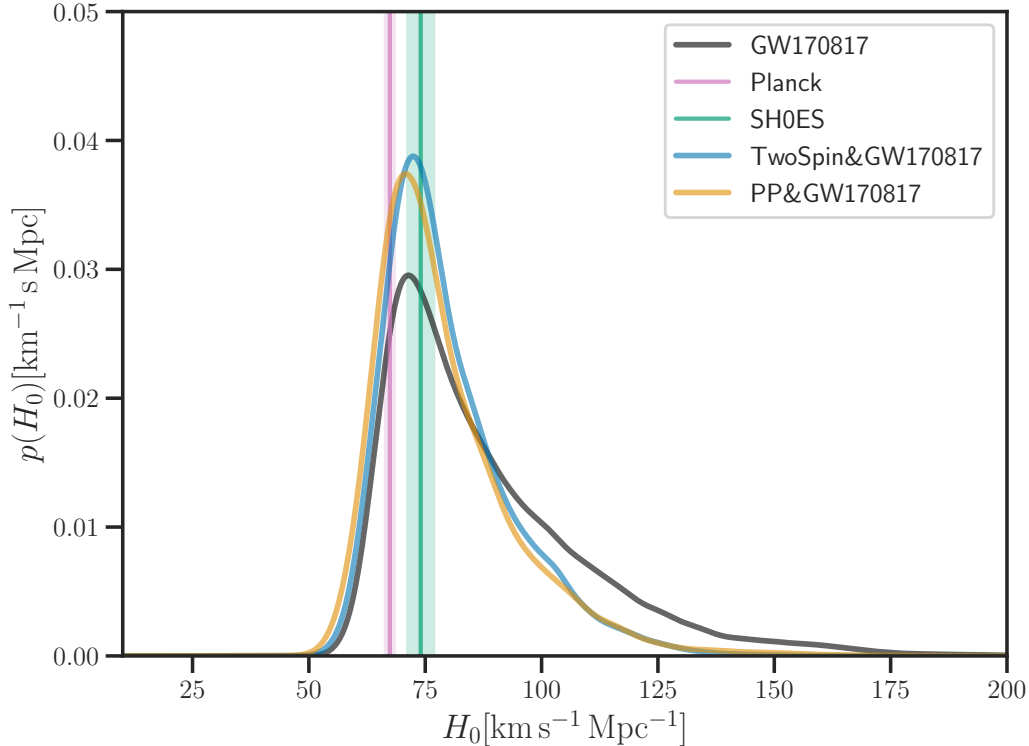


**Figure 3.** Posterior distributions for  $H_0$  obtained by combining the measurements from multi-spectral sirens / spectral sirens with measurement from the bright standard siren GW170817 (Abbott et al. 2017c).

with GWTC-3. Different from the results in this work, as well as our previous works (Wang et al. 2022; Li et al. 2023, 2024), they report the lower-edge of the PIMG to be  $\sim 84M_\odot$  and  $H_0 \sim 36 \text{ Mpc}^{-1} \text{ km s}^{-1}$ . These discrepancies may be driven by the difference in the mass functions between our models and theirs.

1 We thank Yi-Ying Wang and Bo Gao for helpful discussion. This work is supported by the National Natural Science  
 2 Foundation of China (No. 12233011, No. 12203101 and No. 12303056), the Priority Research Program of the Chinese  
 3 Academy of Sciences (No. XDB0550400), and the General Fund of the China Postdoctoral Science Foundation (No.  
 4 2023M733736). This research has made use of data and software obtained from the Gravitational Wave Open Science  
 5 Center (<https://www.gw-openscience.org>), a service of LIGO Laboratory, the LIGO Scientific Collaboration and the  
 6 Virgo Collaboration. LIGO is funded by the U.S. National Science Foundation. Virgo is funded by the French Centre  
 7 National de Recherche Scientifique (CNRS), the Italian Istituto Nazionale della Fisica Nucleare (INFN) and the Dutch  
 8 Nikhef, with contributions by Polish and Hungarian institutes.

*Software:* Bilby (Ashton et al. 2019, version 1.1.4, ascl:1901.011, <https://git.ligo.org/lscsoft/bilby/>), PyMultiNest (Buchner 2016, version 2.11, ascl:1606.005, <https://github.com/JohannesBuchner/PyMultiNest>) Nessai (Williams et al. 2021, 2023; Williams 2021, <https://nessai.readthedocs.io/en/latest/>)

## APPENDIX

### A. ADDITIONAL RESULTS OF TWOSPIN MODEL WITH GWTC-3

Figure 4 displays the posterior distributions of the hyper-parameters inferred by the TwoSpin model using 42 BBHs with  $\text{SNRs} > 11$  in GWTC-3. It shows that both  $m_{\text{max},1}$  and  $m_{\text{max},2}$  are correlated with the Hubble constant. Though



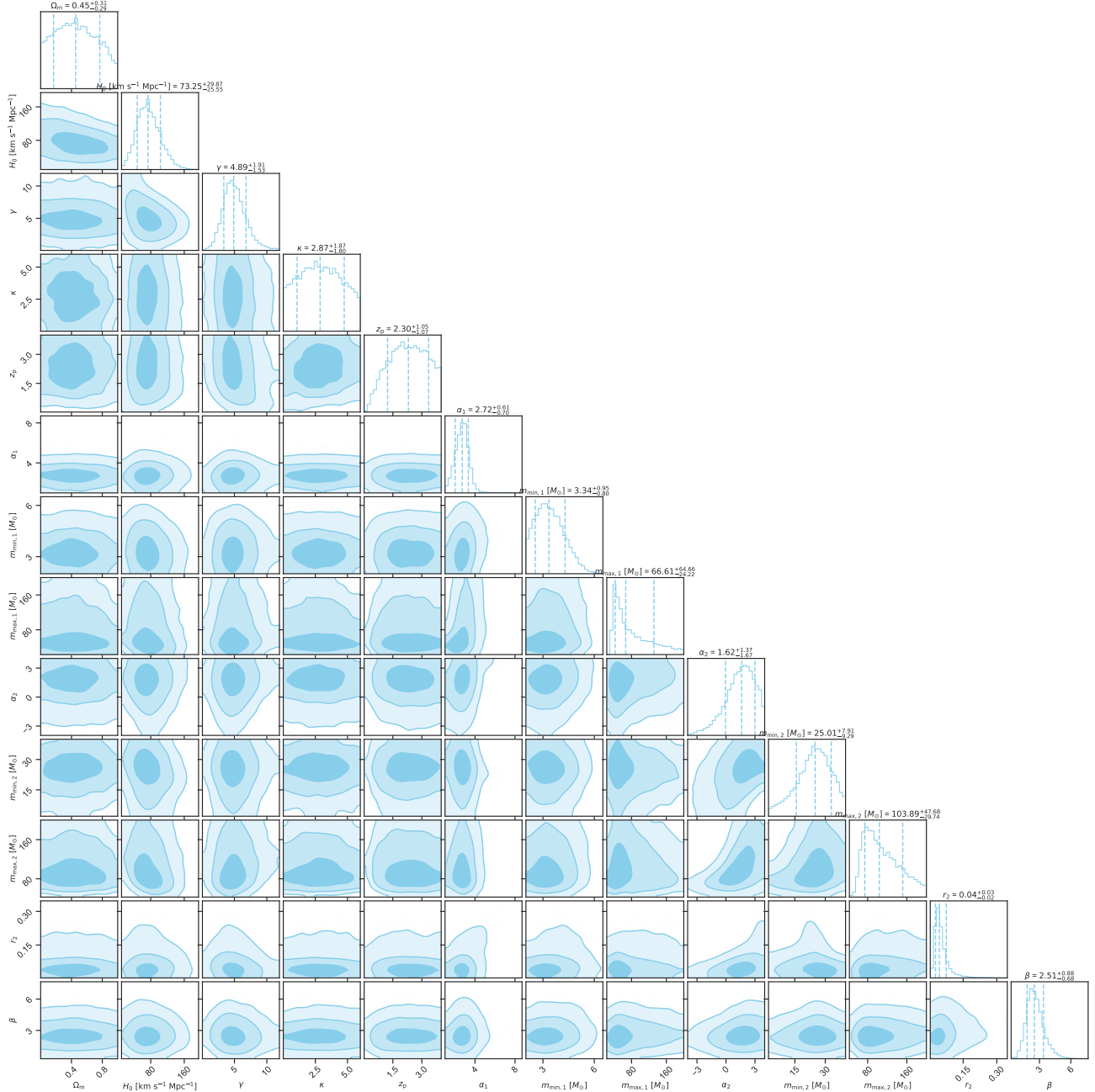


**Figure 4.** Posterior distributions of the hyper-parameters. The dashed lines in the marginal distribution represent the median and 68.3% credible intervals.

the maximum mass of the first-generation sub-population has a tail extend to the higher-mass range, the masses of the 99th and 99.5th percentiles are better constrained and clearly correlated with the Hubble constant, as shown in Figure 5. Figure 6 shows the inferred mass versus spin-magnitude distributions of the two sub-populations, which are consistent with the results obtained with a fixed cosmological model (Li et al. 2023). Following Abbott et al. (2023a), we also perform inference with events selected by  $\text{SNR} > 10$ , as shown in Figure 7.

## B. RESULT WITH POWERLAW+PEAK MODEL

We reproduce the results of the POWERLAW+PEAK model (Abbott et al. 2023a) in our analysis, to ensure the consistency of our framework with theirs. Figure 8 shows the corner plots for the posterior distribution obtained using

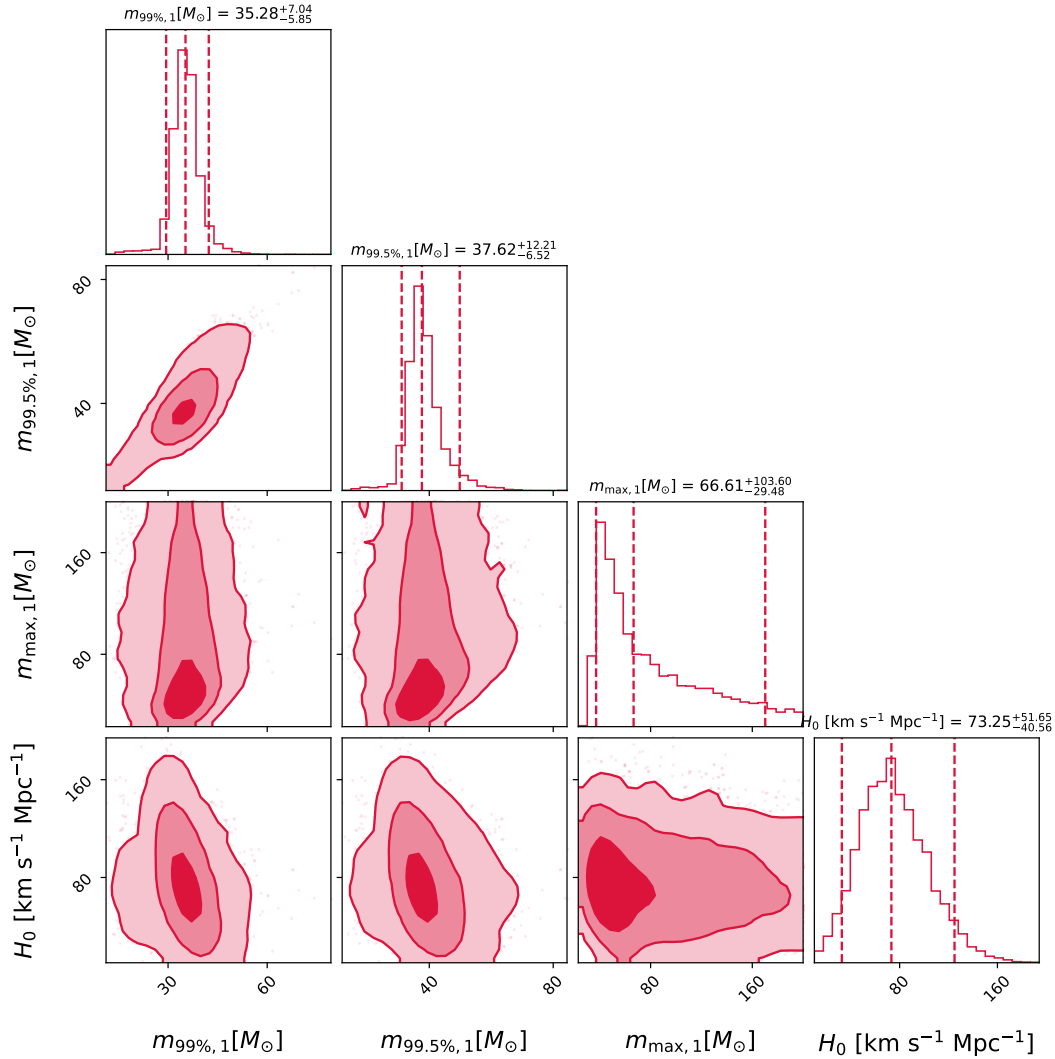


**Figure 5.** Distributions of the Hubble constant, the maximum mass of the first sub-population, and the masses of the 99.5% and 99% percentiles. The dashed lines in the marginal distribution represent the median and 90% credible intervals.

POWERLAW+PEAK model with 42 events selected with SNRs  $> 11$ , which is consistent with that of [Abbott et al. \(2023a\)](#).

## REFERENCES

- Abbott, B. P., Abbott, R., Abbott, T. D., et al. 2017a, *PhRvL*, 119, 161101, doi: [10.1103/PhysRevLett.119.161101](https://doi.org/10.1103/PhysRevLett.119.161101)
- . 2017b, *ApJL*, 848, L12, doi: [10.3847/2041-8213/aa91c9](https://doi.org/10.3847/2041-8213/aa91c9)
- . 2017c, *Nature*, 551, 85, doi: [10.1038/nature24471](https://doi.org/10.1038/nature24471)
- . 2018, *Living Reviews in Relativity*, 21, 3, doi: [10.1007/s41114-018-0012-9](https://doi.org/10.1007/s41114-018-0012-9)
- . 2019, *Physical Review X*, 9, 031040, doi: [10.1103/PhysRevX.9.031040](https://doi.org/10.1103/PhysRevX.9.031040)
- Abbott, R., Abbott, T. D., Abraham, S., et al. 2020, *ApJL*, 896, L44, doi: [10.3847/2041-8213/ab960f](https://doi.org/10.3847/2041-8213/ab960f)
- . 2021a, *ApJL*, 913, L7, doi: [10.3847/2041-8213/abe949](https://doi.org/10.3847/2041-8213/abe949)
- . 2021b, *Physical Review X*, 11, 021053, doi: [10.1103/PhysRevX.11.021053](https://doi.org/10.1103/PhysRevX.11.021053)
- Abbott, R., Abe, H., Acernese, F., et al. 2023a, *ApJ*, 949, 76, doi: [10.3847/1538-4357/ac74bb](https://doi.org/10.3847/1538-4357/ac74bb)
- Abbott, R., Abbott, T. D., Acernese, F., et al. 2023b, *Physical Review X*, 13, 011048, doi: [10.1103/PhysRevX.13.011048](https://doi.org/10.1103/PhysRevX.13.011048)

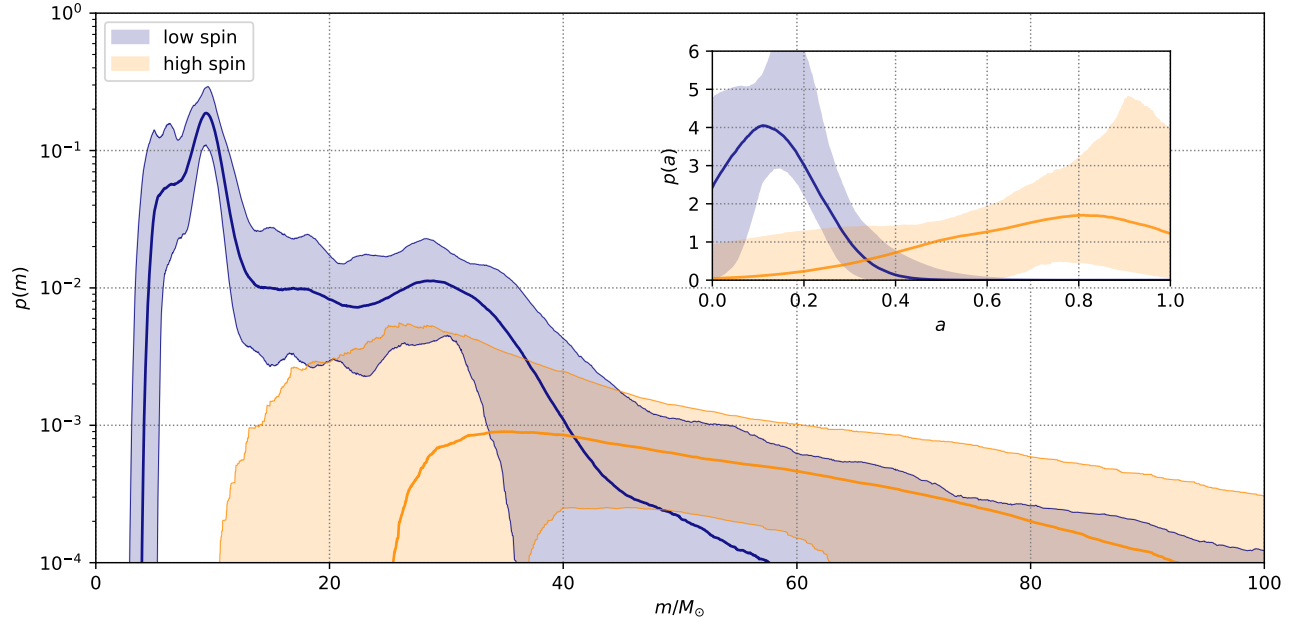


**Figure 6.** Component-mass and spin-magnitude distributions in the multi-spectral sirens, inferred with the TwoSpin model and 42 BBHs with SNRs  $> 11$  in GWTC-3. The solid lines and dashed regions are for the median and 90% credible levels.

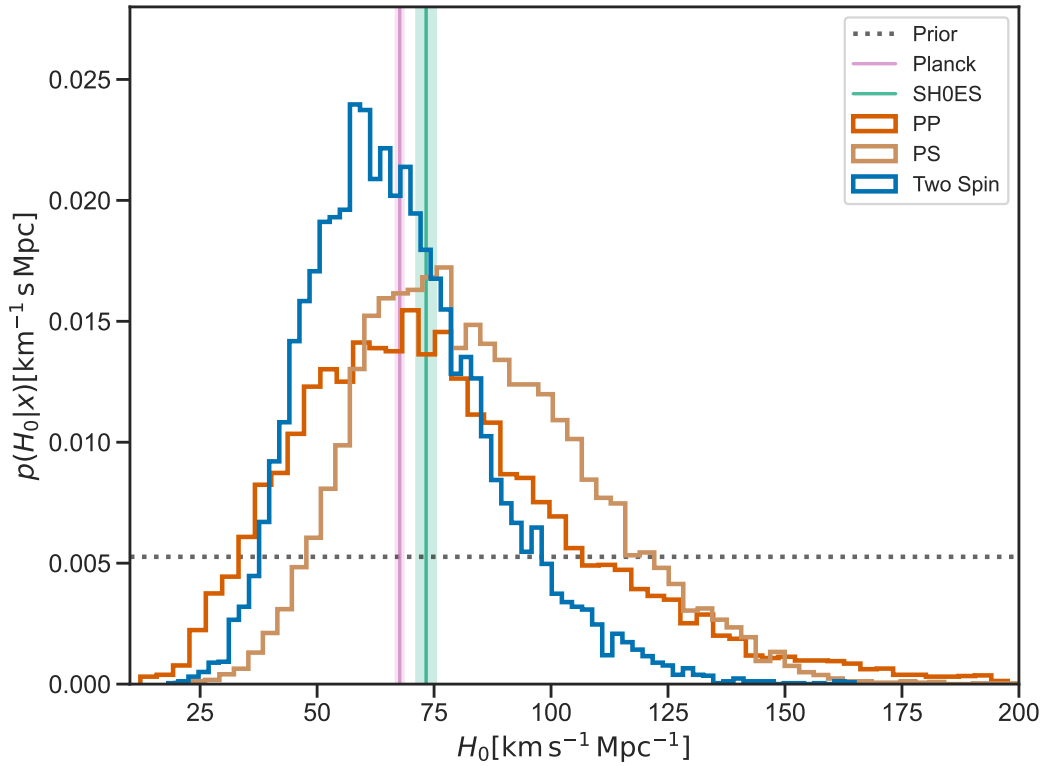


**Figure 7.** The Hubble constant inferred using multi-spectral sirens i.e. the TwoSpin model and the traditional spectral sirens (PP and PS models), with events selected by  $\text{SNR} > 10$ . For reference, the pink and green bands represent the Hubble constant measured from CMB (Planck Collaboration et al. 2016) and that measured in the local universe (Riess et al. 2019), respectively. The dotted line represent the prior distribution.

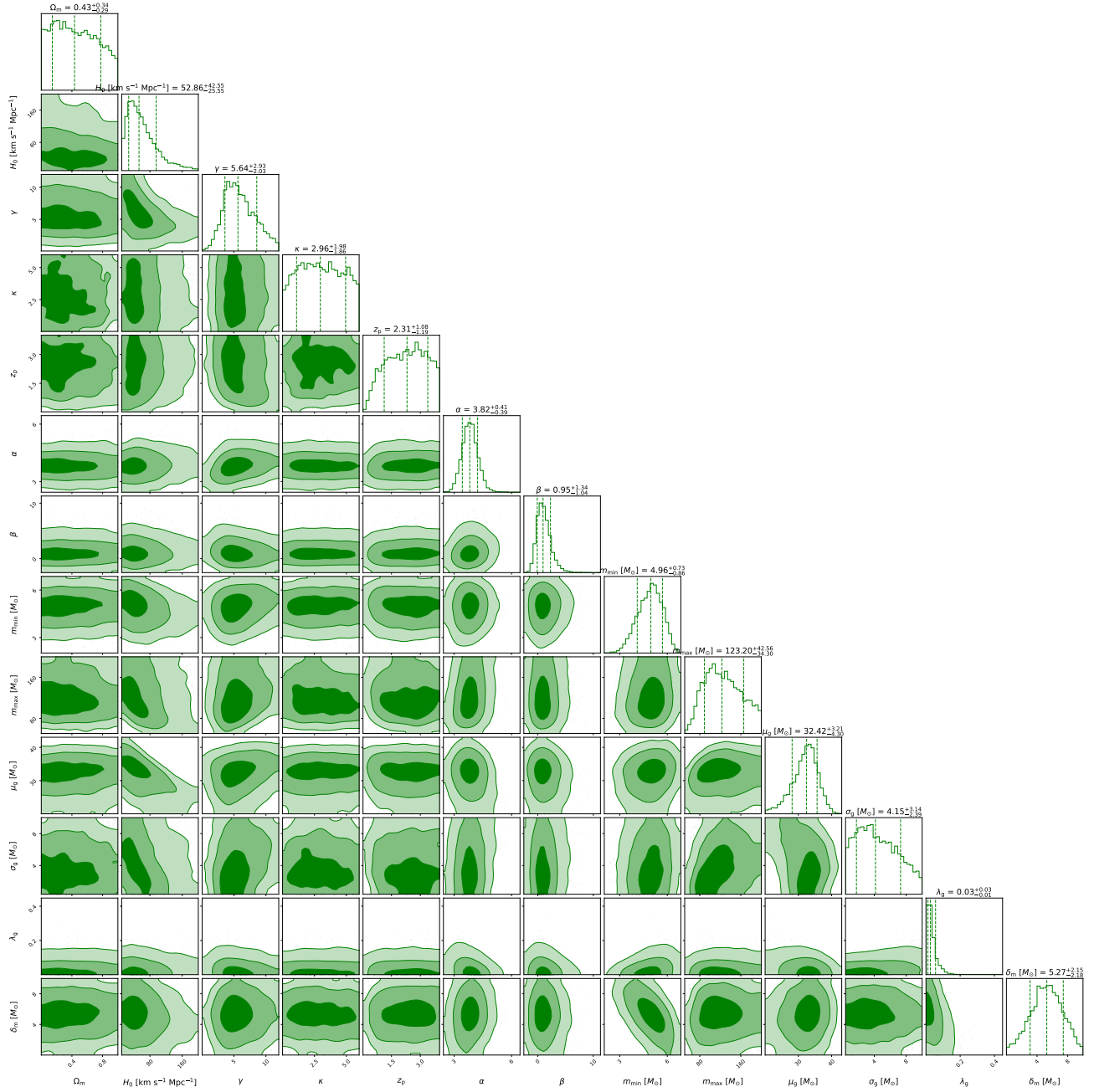


**Figure 8.** Distributions of the parameters for the cosmology model and the POWERLAW+PEAK population model. The dashed lines in the marginal distribution represent the median and 68.3% credible intervals.

- Ashton, G., Hübner, M., Lasky, P. D., et al. 2019, *Bilby*: Bayesian inference library, *Astrophysics Source Code Library*, record ascl:1901.011. <http://ascl.net/1901.011>
- Bailyn, C. D., Jain, R. K., Coppi, P., & Orosz, J. A. 1998, *ApJ*, 499, 367, doi: [10.1086/305614](https://doi.org/10.1086/305614)
- Buchner, J. 2016, *PyMultiNest*: Python interface for MultiNest, *Astrophysics Source Code Library*, record ascl:1606.005. <http://ascl.net/1606.005>
- Callister, T. A., & Farr, W. M. 2024, *Physical Review X*, 14, 021005, doi: [10.1103/PhysRevX.14.021005](https://doi.org/10.1103/PhysRevX.14.021005)
- Cheng, A. Q., Zevin, M., & Vitale, S. 2023, *ApJ*, 955, 127, doi: [10.3847/1538-4357/aced98](https://doi.org/10.3847/1538-4357/aced98)
- Edelman, B., Doctor, Z., Godfrey, J., & Farr, B. 2022, *ApJ*, 924, 101, doi: [10.3847/1538-4357/ac3667](https://doi.org/10.3847/1538-4357/ac3667)
- Ezquiaga, J. M., & Holz, D. E. 2022, *PhRvL*, 129, 061102, doi: [10.1103/PhysRevLett.129.061102](https://doi.org/10.1103/PhysRevLett.129.061102)
- Farah, A., Fishbach, M., Essick, R., Holz, D. E., & Galaudage, S. 2022, *ApJ*, 931, 108, doi: [10.3847/1538-4357/ac5f03](https://doi.org/10.3847/1538-4357/ac5f03)
- Farah, A. M., Callister, T. A., María Ezquiaga, J., Zevin, M., & Holz, D. E. 2024, arXiv e-prints, arXiv:2404.02210, doi: [10.48550/arXiv.2404.02210](https://doi.org/10.48550/arXiv.2404.02210)
- Farah, A. M., Edelman, B., Zevin, M., et al. 2023, *ApJ*, 955, 107, doi: [10.3847/1538-4357/aced02](https://doi.org/10.3847/1538-4357/aced02)
- Farmer, R., Renzo, M., de Mink, S. E., Marchant, P., & Justham, S. 2019, *ApJ*, 887, 53, doi: [10.3847/1538-4357/ab518b](https://doi.org/10.3847/1538-4357/ab518b)
- Farr, W. M., Fishbach, M., Ye, J., & Holz, D. E. 2019, *ApJL*, 883, L42, doi: [10.3847/2041-8213/ab4284](https://doi.org/10.3847/2041-8213/ab4284)
- Farr, W. M., Sravan, N., Cantrell, A., et al. 2011, *ApJ*, 741, 103, doi: [10.1088/0004-637X/741/2/103](https://doi.org/10.1088/0004-637X/741/2/103)
- Fishbach, M., & Holz, D. E. 2020, *ApJL*, 891, L27, doi: [10.3847/2041-8213/ab7247](https://doi.org/10.3847/2041-8213/ab7247)
- Fishbach, M., Holz, D. E., & Farr, B. 2017, *ApJL*, 840, L24, doi: [10.3847/2041-8213/aa7045](https://doi.org/10.3847/2041-8213/aa7045)
- Galaudage, S., Talbot, C., Nagar, T., et al. 2021, *ApJL*, 921, L15, doi: [10.3847/2041-8213/ac2f3c](https://doi.org/10.3847/2041-8213/ac2f3c)
- Gao, S.-J., Li, X.-D., & Shao, Y. 2022, *MNRAS*, 514, 1054, doi: [10.1093/mnras/stac1426](https://doi.org/10.1093/mnras/stac1426)
- Gerosa, D., & Berti, E. 2017, *PhRvD*, 95, 124046, doi: [10.1103/PhysRevD.95.124046](https://doi.org/10.1103/PhysRevD.95.124046)
- Gerosa, D., & Fishbach, M. 2021, *Nature Astronomy*, 5, 749, doi: [10.1038/s41550-021-01398-w](https://doi.org/10.1038/s41550-021-01398-w)
- Godfrey, J., Edelman, B., & Farr, B. 2023, arXiv e-prints, arXiv:2304.01288, doi: [10.48550/arXiv.2304.01288](https://doi.org/10.48550/arXiv.2304.01288)
- Golomb, J., & Talbot, C. 2023, *PhRvD*, 108, 103009, doi: [10.1103/PhysRevD.108.103009](https://doi.org/10.1103/PhysRevD.108.103009)
- Guo, W.-H., Li, Y.-J., Wang, Y.-Z., et al. 2024, arXiv e-prints, arXiv:2406.03257, doi: [10.48550/arXiv.2406.03257](https://doi.org/10.48550/arXiv.2406.03257)
- Gupta, A., Gerosa, D., Arun, K. G., et al. 2020, *PhRvD*, 101, 103036, doi: [10.1103/PhysRevD.101.103036](https://doi.org/10.1103/PhysRevD.101.103036)
- Holz, D. E., & Hughes, S. A. 2005, *ApJ*, 629, 15, doi: [10.1086/431341](https://doi.org/10.1086/431341)
- Iacovelli, F., Mancarella, M., Foffa, S., & Maggiore, M. 2022a, *ApJS*, 263, 2, doi: [10.3847/1538-4365/ac9129](https://doi.org/10.3847/1538-4365/ac9129)
- . 2022b, *ApJ*, 941, 208, doi: [10.3847/1538-4357/ac9cd4](https://doi.org/10.3847/1538-4357/ac9cd4)
- Kalogera, V., & Baym, G. 1996, *ApJL*, 470, L61, doi: [10.1086/310296](https://doi.org/10.1086/310296)
- Karathanasis, C., Mukherjee, S., & Mastrogiovanni, S. 2023, *MNRAS*, 523, 4539, doi: [10.1093/mnras/stad1373](https://doi.org/10.1093/mnras/stad1373)
- Kimball, C., Talbot, C., Berry, C. P. L., et al. 2021, *ApJL*, 915, L35, doi: [10.3847/2041-8213/ac0aef](https://doi.org/10.3847/2041-8213/ac0aef)
- Li, Y.-J., Tang, S.-P., Gao, S.-J., Wu, D.-C., & Wang, Y.-Z. 2024, arXiv e-prints, arXiv:2404.09668, doi: [10.48550/arXiv.2404.09668](https://doi.org/10.48550/arXiv.2404.09668)
- Li, Y.-J., Tang, S.-P., Wang, Y.-Z., et al. 2021a, *ApJ*, 923, 97, doi: [10.3847/1538-4357/ac3440](https://doi.org/10.3847/1538-4357/ac3440)
- Li, Y.-J., Wang, Y.-Z., Han, M.-Z., et al. 2021b, *ApJ*, 917, 33, doi: [10.3847/1538-4357/ac0971](https://doi.org/10.3847/1538-4357/ac0971)
- Li, Y.-J., Wang, Y.-Z., Tang, S.-P., & Fan, Y.-Z. 2023, arXiv e-prints, arXiv:2303.02973, doi: [10.48550/arXiv.2303.02973](https://doi.org/10.48550/arXiv.2303.02973)
- Li, Y.-J., Wang, Y.-Z., Tang, S.-P., et al. 2022, *ApJL*, 933, L14, doi: [10.3847/2041-8213/ac78dd](https://doi.org/10.3847/2041-8213/ac78dd)
- Madau, P., & Dickinson, M. 2014, *ARA&A*, 52, 415, doi: [10.1146/annurev-astro-081811-125615](https://doi.org/10.1146/annurev-astro-081811-125615)
- Magaña Hernandez, I., & Ray, A. 2024, arXiv e-prints, arXiv:2404.02522, doi: [10.48550/arXiv.2404.02522](https://doi.org/10.48550/arXiv.2404.02522)
- Mapelli, M., Giacobbo, N., Ripamonti, E., & Spera, M. 2017, *MNRAS*, 472, 2422, doi: [10.1093/mnras/stx2123](https://doi.org/10.1093/mnras/stx2123)
- Mastrogiovanni, S., Leyde, K., Karathanasis, C., et al. 2021, *PhRvD*, 104, 062009, doi: [10.1103/PhysRevD.104.062009](https://doi.org/10.1103/PhysRevD.104.062009)
- O’Leary, R. M., Meiron, Y., & Kocsis, B. 2016, *ApJL*, 824, L12, doi: [10.3847/2041-8205/824/1/L12](https://doi.org/10.3847/2041-8205/824/1/L12)
- Özel, F., Psaltis, D., Narayan, R., & McClintock, J. E. 2010, *ApJ*, 725, 1918, doi: [10.1088/0004-637X/725/2/1918](https://doi.org/10.1088/0004-637X/725/2/1918)
- Pierra, G., Mastrogiovanni, S., & Perriès, S. 2024a, arXiv e-prints, arXiv:2406.01679, doi: [10.48550/arXiv.2406.01679](https://doi.org/10.48550/arXiv.2406.01679)
- Pierra, G., Mastrogiovanni, S., Perriès, S., & Mapelli, M. 2024b, *PhRvD*, 109, 083504, doi: [10.1103/PhysRevD.109.083504](https://doi.org/10.1103/PhysRevD.109.083504)
- Planck Collaboration, Ade, P. A. R., Aghanim, N., et al. 2016, *A&A*, 594, A13, doi: [10.1051/0004-6361/201525830](https://doi.org/10.1051/0004-6361/201525830)
- Planck Collaboration, Aghanim, N., Akrami, Y., et al. 2020, *A&A*, 641, A6, doi: [10.1051/0004-6361/201833910](https://doi.org/10.1051/0004-6361/201833910)
- Pratten, G., García-Quirós, C., Colleoni, M., et al. 2021, *PhRvD*, 103, 104056, doi: [10.1103/PhysRevD.103.104056](https://doi.org/10.1103/PhysRevD.103.104056)

- Ray, A., Magaña Hernandez, I., Breivik, K., & Creighton, J. 2024, arXiv e-prints, arXiv:2404.03166, doi: [10.48550/arXiv.2404.03166](https://doi.org/10.48550/arXiv.2404.03166)
- Rhoades, C. E., & Ruffini, R. 1974, *PhRvL*, 32, 324, doi: [10.1103/PhysRevLett.32.324](https://doi.org/10.1103/PhysRevLett.32.324)
- Riess, A. G., Casertano, S., Yuan, W., Macri, L. M., & Scolnic, D. 2019, *ApJ*, 876, 85, doi: [10.3847/1538-4357/ab1422](https://doi.org/10.3847/1538-4357/ab1422)
- Schutz, B. F. 1986, *Nature*, 323, 310, doi: [10.1038/323310a0](https://doi.org/10.1038/323310a0)
- Taylor, S. R., Gair, J. R., & Mandel, I. 2012, *PhRvD*, 85, 023535, doi: [10.1103/PhysRevD.85.023535](https://doi.org/10.1103/PhysRevD.85.023535)
- The LIGO, V., & collaborations, K. 2021, Data distribution of Constraints on the cosmic expansion history from the GWTC-3, Zenodo, doi: [10.5281/zenodo.5645777](https://doi.org/10.5281/zenodo.5645777)
- The LIGO Scientific Collaboration, the Virgo Collaboration, & the KAGRA Collaboration. 2024, arXiv e-prints, arXiv:2404.04248, doi: [10.48550/arXiv.2404.04248](https://doi.org/10.48550/arXiv.2404.04248)
- The LIGO Scientific Collaboration, the Virgo Collaboration, Abbott, R., et al. 2021a, arXiv e-prints, arXiv:2108.01045, doi: [10.48550/arXiv.2108.01045](https://doi.org/10.48550/arXiv.2108.01045)
- The LIGO Scientific Collaboration, the Virgo Collaboration, the KAGRA Collaboration, et al. 2021b, arXiv e-prints, arXiv:2111.03606, doi: [10.48550/arXiv.2111.03606](https://doi.org/10.48550/arXiv.2111.03606)
- Tiwari, V. 2022, *ApJ*, 928, 155, doi: [10.3847/1538-4357/ac589a](https://doi.org/10.3847/1538-4357/ac589a)
- . 2024, *MNRAS*, 527, 298, doi: [10.1093/mnras/stad3155](https://doi.org/10.1093/mnras/stad3155)
- Toubiana, A., Katz, M. L., & Gair, J. R. 2023, *MNRAS*, 524, 5844, doi: [10.1093/mnras/stad2215](https://doi.org/10.1093/mnras/stad2215)
- Ulrich, Y., Croon, D., Sakstein, J., & McDermott, S. 2024, arXiv e-prints, arXiv:2406.06109, doi: [10.48550/arXiv.2406.06109](https://doi.org/10.48550/arXiv.2406.06109)
- Verde, L., Treu, T., & Riess, A. G. 2019, *Nature Astronomy*, 3, 891, doi: [10.1038/s41550-019-0902-0](https://doi.org/10.1038/s41550-019-0902-0)
- Vink, J. S., Higgins, E. R., Sander, A. A. C., & Sabhahit, G. N. 2021, *MNRAS*, 504, 146, doi: [10.1093/mnras/stab842](https://doi.org/10.1093/mnras/stab842)
- Wang, Y.-Y., Tang, S.-P., Jin, Z.-P., & Fan, Y.-Z. 2023, *ApJ*, 943, 13, doi: [10.3847/1538-4357/aca96c](https://doi.org/10.3847/1538-4357/aca96c)
- Wang, Y.-Z., Li, Y.-J., Vink, J. S., et al. 2022, *ApJL*, 941, L39, doi: [10.3847/2041-8213/aca89f](https://doi.org/10.3847/2041-8213/aca89f)
- Wang, Y.-Z., Tang, S.-P., Liang, Y.-F., et al. 2021, *ApJ*, 913, 42, doi: [10.3847/1538-4357/abf5df](https://doi.org/10.3847/1538-4357/abf5df)
- Williams, M. J. 2021, nessai: Nested Sampling with Artificial Intelligence, latest, Zenodo, doi: [10.5281/zenodo.4550693](https://doi.org/10.5281/zenodo.4550693)
- Williams, M. J., Veitch, J., & Messenger, C. 2021, *Phys. Rev. D*, 103, 103006, doi: [10.1103/PhysRevD.103.103006](https://doi.org/10.1103/PhysRevD.103.103006)
- . 2023. <https://arxiv.org/abs/2302.08526>
- Woosley, S. E. 2017, *ApJ*, 836, 244, doi: [10.3847/1538-4357/836/2/244](https://doi.org/10.3847/1538-4357/836/2/244)
- Woosley, S. E., & Heger, A. 2021, *ApJL*, 912, L31, doi: [10.3847/2041-8213/abf2c4](https://doi.org/10.3847/2041-8213/abf2c4)
- You, Z.-Q., Zhu, X.-J., Ashton, G., Thrane, E., & Zhu, Z.-H. 2021, *ApJ*, 908, 215, doi: [10.3847/1538-4357/abd4d4](https://doi.org/10.3847/1538-4357/abd4d4)
- Zevin, M., Bavera, S. S., Berry, C. P. L., et al. 2021, *ApJ*, 910, 152, doi: [10.3847/1538-4357/abe40e](https://doi.org/10.3847/1538-4357/abe40e)